EASR

Engineering and Applied Science Research

https://www.tci-thaijo.org/index.php/easr/index

Published by the Faculty of Engineering, Khon Kaen University, Thailand

Effect of (Cr, Fe)-substitution at B sites of $CuB_{1-x}(Cr_{1/2}Fe_{1/2})_xO_2$ delafossite oxides on optical, magnetic, and dielectric properties

Sornamol Traiphop and Teerasak Kamwanna*

Department of Physics, Faculty of Science, Khon Kaen University, Khon Kaen 40002, Thailand

Received 19 March 2021
Revised 23 April 2021
Accepted 14 May 2021

Abstract

In this work, we report room temperature ferromagnetic and colossal dielectric behavior in delafossite oxides of $CuB_{1-x}(Cr_{1/2}Fe_{1/2})_xO_2$ with $x = 0.01$ and 0.03. All samples were synthesized by the solid-state reaction method. The microstructure, optical, magnetic, and dielectric properties were investigated by X-ray diffraction (XRD), scanning electron microscope (SEM), UV-visible spectroscopy, vibrating sample magnetometer (VSM), and impedance analyzer, respectively. The crystal structure of all samples was found to be of the R-3m delafossite structure, while their particle size was ~ 300 nm in the undoped sample ($x = 0$) and slightly increased with increasing x value. Regarding their optical properties, we observed the absorbance peak at wavelength ~250 nm corresponding to the direct optical band gap of about 2.90, 2.88, and 2.85 eV for sample $x = 0.00$, 0.01, and 0.03, respectively. The magnetic properties of the doped samples ($x = 0.01$ and 0.03) exhibited a ferromagnetic behavior at room temperature with a finite coercivity of about ~300 Oe. Furthermore, the magnetization of this $CuB_{1-x}(Cr_{1/2}Fe_{1/2})_xO_2$ delafossite is increased with increasing x value. Finally, the dielectric measurements revealed that Cr plays a role in maintaining the dielectric permittivity of the $CuB_{1-x}(Cr_{1/2}Fe_{1/2})_xO_2$ samples.

Keywords: Delafossite oxides, $CuBO_2$, Magnetic properties, Dielectric properties

1. Introduction

Delafossite oxide is a ternary oxide that has a chemical formula of AMO_2 where A = Cu, Ag, Pd, Pt and M = Cr, Fe, Al, B, etc. For the past decade, the Cu-based delafossite ($CuMO_2$) has been studied for transparent conducting oxides (TCOs) applications due to its good p-type conductivity and high transparency to visible light [1, 2]. To increase its conductivity, the M cation is substitutionally doped [3]. By doing so, the magnetic properties of these materials can change from nonmagnetic to magnetic [4-7]. As a result of the combination of unique electrical, optical, and magnetic properties, they have emerged as a new class of materials with great potential for application in diluted magnetic semiconductors (DMSs), such as spintronic devices, spin-valve transistors, and nonvolatile logic devices. Cu-based delafossite members, such as $CuCrO_2$, $CuFeO_2$, and $CuAlO_2$ become mainstream which was studied for DMSs materials contrary to the $CuBO_2$. However, the $CuBO_2$ has been found to possess high electrical conductivity and transparency, which can be comparable to that of other members as reported by Snure and Tiwari [8]. Furthermore, this material was studied in several fields, such as UV photocatalyst [9, 10], electron field emitter [11-13], hydrolysis reaction catalyst [14], and photovoltaic [15]. In our previous work, ferromagnetic behavior of $CuBO_2$ doped with Fe at room temperature was observed [16].

Over the last few years, the colossal dielectric permittivity of Cu-based delafossite has been reported in the literature [17-20]. Moreover, coexistence of the ferromagnetic and colossal dielectric behaviors at room temperature was observed in $CuCo_{1/2}Ti_{1/2}O_2$ [21]. The interesting properties of these materials are a focus of much research due to their enormous applications particularly in future electronic devices.

In this work, Cr and Fe co-doped $CuBO_2$ having the chemical composition of $CuB_{1-x}(Cr_{1/2}Fe_{1/2})_xO_2$ with $x = 0.00$, 0.01, and 0.03 was synthesized by the solid state reaction method. The microstructural, optical, magnetic, and dielectric properties were investigated and discussed.

2. Materials and methods

2.1 Sample preparation

The $CuB_{1-x}(Cr_{1/2}Fe_{1/2})_xO_2$ ($x = 0.00$, 0.01 and 0.03) powders were prepared by the solid-state reaction method. High-purity powders of CuO (Alfa Aesar, purity 99%), H_3BO_3 (Aldrich, purity 99.5%), Cr_2O_3 (Aldrich, purity 98.5%), and Fe_2O_3 (Aldrich, 99%) were used as starting materials. All starting powders were mixed to form a stoichiometric mixture. Then, the mixed powders were ball-milled for 24 h by using zirconia balls in the ethanol medium. The resulting powders were dried on a hot plate at a temperature of about 100 °C overnight. The dried powders were calcined in air at a temperature of 805 °C for 1 h. For the dielectric measurement, the calcined

*Corresponding author. Tel.: +668 4610 9597
Email address: teekam@kku.ac.th
doi: 10.14456/easr.2021.72

powders were ground and pressed into pellets of ~1 mm in thickness and ~10 mm in diameter by uniaxial compression, and then sintered in air at 900 °C for 6 h. Finally, the pellets were coated with Au on both sides.

2.2 Characterization

The crystal structure and phase composition of the $CuB_{1-x}(Cr_{1/2}Fe_{1/2})_xO_2$ (x = 0.00, 0.01, and 0.03) powders were examined by using an X-ray diffractometer (PANalytical, EMPYREAN) and measurements were taken between 20° to 80°. The morphology of the calcined powders was observed via Field-emission Scanning Electron Microscopy (FE-SEM, FEI, Helios NanoLab G3 CX). The UV-Vis-NIR scanning spectrophotometry (Shimadzu UV-3101PC) was employed to obtain optical absorption spectra of the samples in the range of 200 to 700 nm. The magnetic properties were characterized by using a Quantum Design VersaLab 3 T cryogen-free system equipped with a vibrating sample magnetometer (VSM) at room temperature. For the dielectric measurement, a KEYSIGHT E4990A Impedance Analyzer was used to measure the capacitance (Cp) and the dissipation factor (tanδ) over the frequency range of 40 - 3×10^6 Hz at room temperature.

3. Results and discussion

3.1 Structural characterization

XRD Patterns at room temperature for the $CuB_{1-x}(Cr_{1/2}Fe_{1/2})_xO_2$ (x = 0.00, 0.01 and 0.03) powders are shown in Figure 1. All patterns were identical, corresponding with what was observed in previous reports. This suggests a pure polycrystalline phase with a delafossite structure (space group: R-3m) was acquired in all samples. According to the lattice parameter calculation, lattice constants a for x = 0.00, 0.01, and 0.03 are 3.0180, 3.0180, and 3.0178 A, respectively, while lattice constants c are 17.0422, 17.0378, and 17.0411 A, respectively. The a and c values were found to vary slightly from those reported by Santra et al. [13]. We also observed a slight decrease in extracted lattice parameter c with increasing Cr and Fe content. This means that the O–Cu–O dumbbells along the c-axis shrink as a result of the co-doping suggesting that structural modulation at the triangular lattice occurred in the $CuB_{1-x}(Cr_{1/2}Fe_{1/2})_xO_2$ samples.

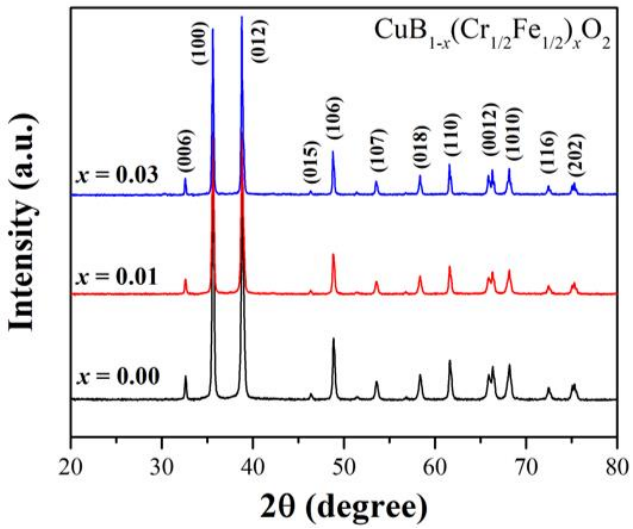

Figure 1 XRD Pattern of calcined $CuB_{1-x}(Cr_{1/2}Fe_{1/2})_xO_2$ powders with x value of 0.00, 0.01, and 0.03.

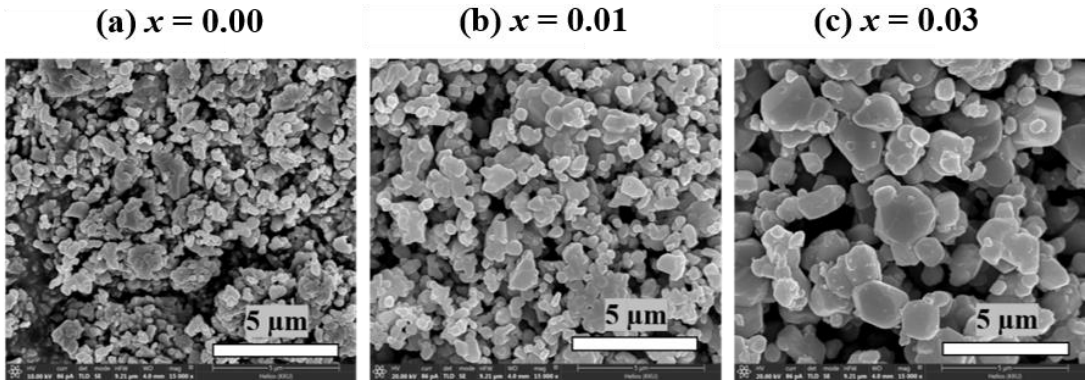

Figure 2 SEM Image of calcined $CuB_{1-x}(Cr_{1/2}Fe_{1/2})_xO_2$ powders where x is (a) 0.00, (b) 0.01, and (c) 0.03

The morphology of the calcined $CuB_{1-x}(Cr_{1/2}Fe_{1/2})_xO_2$ powders is shown in SEM images in Figure 2. The hexagonal-like shape was obtained in all samples. Fe and Cr were found to have an effect on crystal growth with particles of the undoped sample (x=0.00) being ~300 nm in diameter (Figure 2a), and an increase in particle size observed with increasing x value (~ 1000 nm for x = 0.03 in Figure 2c).

3.2 Optical properties

Optical properties were studied by UV-Vis-NIR scanning spectrophotometry. Figure 3a shows an optical absorption spectrum of the $CuB_{1-x}(Cr_{1/2}Fe_{1/2})_xO_2$ powders over the wavelength range of 200-700 nm at room temperature. From the spectrum, a strong absorption peak was observed at the UV range (~ 250 nm) with low absorption in the visible and near-IR region (300-800 nm). This peak can be attributed to electron excitation from the valence band to the conduction band. To evaluate the direct optical band gap (E_g) of the sample, the Tauc's relation was employed. This relation can be expressed as $(ahv)^2 = A(hv - E_g)$, where a is the absorption coefficient, hv is the incident photon energy, and A is the constant. The E_g value can be obtained from a plot between $(ahv)^2$ vs hv. The extrapolation of the linear portion of the graph to the hv axis revealed E_g of the samples. In Figure 3b, the direct optical band gap values of the samples with x = 0.00, 0.01, and 0.03 were found to be 2.91, 2.88, and 2.85 eV, respectively. This implies that Fe^{3+} and Cr^{3+} substitution for B^{3+} in $CuBO_2$ can effectively the direct optical band gap.

As can be seen, the increase in the red-shift of E_g is associated with increasing x value. Three factors influence the red shift, (i) the quantum size effect. (ii) the surface effect, and (iii) the interfacial polaron effect. If the particle size increases, the quantum size effect and surface effect will be weakened leading to a red shift of E_g. For the interfacial polaron effect, the E_g red shift occur as a result of an increase in the electron-phonon coupling coefficient [5, 22]. In our samples, the red shift of E_g can be ascribed to the increased particle size in the SEM image, and the interfacial polaron effect introduced in the $CuB_{1-x}(Cr_{1/2}Fe_{1/2})_xO_2$ samples, as detailed in Section 3.4.

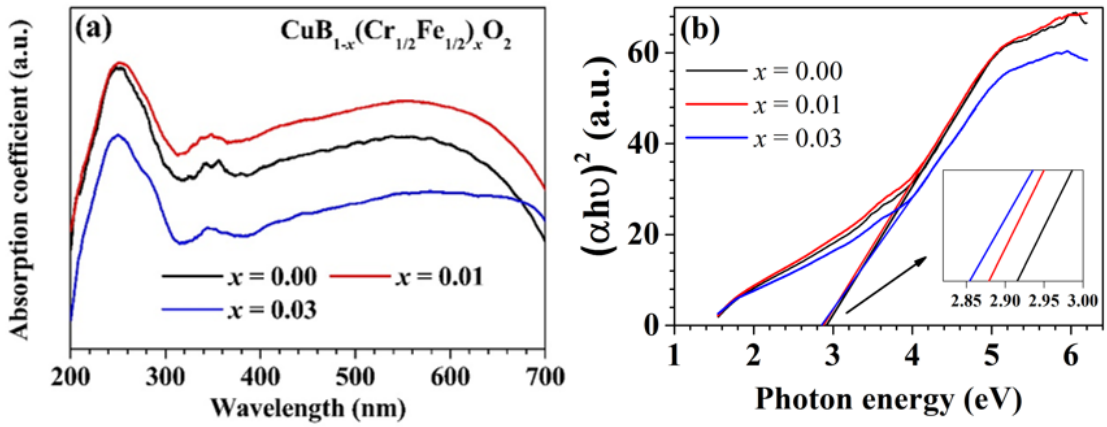

Figure 3 (a) The absorption spectra of calcined $CuB_{1-x}(Cr_{1/2}Fe_{1/2})_xO_2$ powders**.** (b) Tauc's relation of $CuB_{1-x}(Cr_{1/2}Fe_{1/2})_xO_2$ powders**.**

3.3 Magnetic properties

We used a vibrating sample magnetometer (VSM) to examine the magnetic properties of the $CuB_{1-x}(Cr_{1/2}Fe_{1/2})_xO_2$ powders. The magnetization versus magnetic field (*M-H* curve) was performed at room temperature (300K) under an applied magnetic field of $30 \leq H \leq 30$ kOe. The results are shown in Figure 4. For the undoped sample ($x = 0.00$), the magnetization is linearly dependent on the applied magnetic field indicative of a paramagnetic behavior for the $CuBO_2$ sample. On other hand, the co-doped samples ($x = 0.01$ and 0.03) respond to the applied magnetic field in a ferromagnetic fashion i.e. a hysteresis loop was observed. As seen here, the saturation magnetization (M_s) increases almost linearly with increasing x value, indicating that when B^{3+} is substituted by Cr^{3+}/Fe^{3+}, this delafossite oxide undergoes a change affecting its magnetic properties in a mixed manner.

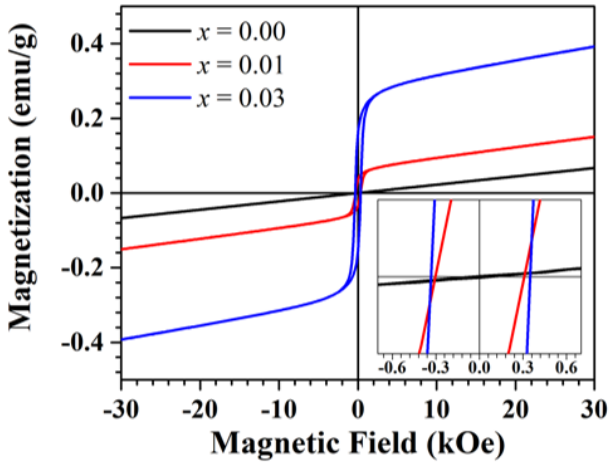

Figure 4 M-H Curves of calcined $CuB_{1-x}(Cr_{1/2}Fe_{1/2})_xO_2$ powders measured at 300K**.**

To describe the effect of Cr and Fe substitution on the magnetic transition in $CuBO_2$, the $CuBO_2$ delafossite structure should be considered. In the structure, Cu^+ is linearly coordinated with two O^{2-}, resembling a O–Cu–O dumbbell shape along the *c*-axis. This leads to formation of a layered triangular lattice anti-ferromagnetic structure. Specifically, each of the O^{2-} in the O–Cu–O dumbbells is linked with three B^{3+} ions parallel to the *ab* plane. Therefore, the partial substitution at the B^{3+} site with a metal (M) cation of different ionic radius would structurally modify the triangular lattice. This leads to multiferroic phase formation. The reduction in the lattice parameter *c*, in this work, is the cause of the strengthened distortion of the BO_6 octahedral, in turn leading to shrinkage of the O–Cu–O dumbbells. The observed magnetic behavior of $CuB_{1-x}(Cr_{1/2}Fe_{1/2})_xO_2$ is likely as a result of this structural modification.

Additionally, through the approximately 180° angled M–O–M linkages, the M cations in the delafossite structure interact with each other. It is expected that these linkages play a dominant role in the anti-ferromagnetic behavior of these materials. The combination of the number of M–M pairs and M–M distances is known to produce results with the magnetic exchange interaction. In this case, B^{3+}–Cr^{3+} and B^{3+}–Fe^{3+} super-exchange interactions lead therefore to ferromagnetism. The anti-ferromagnetic B^{3+}–B^{3+} coupling is dominated by the ferromagnetic B^{3+}–Cr^{3+} and B^{3+}–Fe^{3+} coupling dominates, resulting in a rise in ferromagnetism.

A further increase in Cr and Fe concentration results in a greater number of B^{3+}–Cr^{3+} and B^{3+}–Fe^{3+} pairs. This indicates that the ferromagnetic B^{3+}–Cr^{3+} and B^{3+}–Fe^{3+} couplings would be increased. On the other hand, anti-ferromagnetic B^{3+}–B^{3+} coupling would be weakened. According to the XRD measurements, lattice parameter *c* decreases with increasing Cr and Fe concentration. Thus, it is certain that the decreases correspond to only shorter B^{3+}–Cr^{3+} and B^{3+}–Fe^{3+} bond distances, which influences the B^{3+}–Cr^{3+} and B^{3+}–Fe^{3+} interaction. As a result, the long-range B^{3+}–B^{3+} interactions are likely associated with anti-ferromagnetism coupled with short-range B^{3+}–Cr^{3+} and B^{3+}–Fe^{3+} ferromagnetism in the $CuB_{1-x}(Cr_{1/2}Fe_{1/2})_xO_2$ system. From this analysis, it is concluded that the competition between the number of the M–M pairs and shorter M–M distances results in significantly higher magnetization when Cr and Fe concentration is increased in the $CuBO_2$ system.

3.4 Dielectric properties

The $CuB_{1-x}(Cr_{1/2}Fe_{1/2})_xO_2$ ceramics were investigated for their dielectric properties, as shown in Figure 5. The measurement was done at room temperature in the frequency range of 40-3×10^6 Hz,. Noticeably, all ceramic samples exhibit giant dielectric properties with dielectric permittivity (ε′) of about 10^4–10^5 in a low-frequency range. The ε′ values at room temperature and 1 kHz of the ceramic sample $x = 0.00$, 0.01, and 0.03 are about 24,828, 16,129, and 94,720, respectively. This high ε′ value of the $CuB_{1-x}(Cr_{1/2}Fe_{1/2})_xO_2$ ceramics is of comparable value to what were measured in such giant dielectric materials as $CaCu_3Ti_4O_{12}$, CuO, and co-doped TiO_2 ceramics [23-25]. Likely, there is an association between the resulting giant dielectric permittivity and the extrinsic effect of the insulating grain boundary (GB) and/or sample-electrode interface contact effect [26]. However, the ε′ of the co-doped samples decrease in a step-like manner when the frequency is increased above 10^4 Hz. This behavior gives rise to the presence of the peak of dielectric loss tangent (tanδ) at a frequency of about 10^5 Hz, as shown in Figure 6. It is generally a result of energy loss caused by the process of dielectric relaxation process.

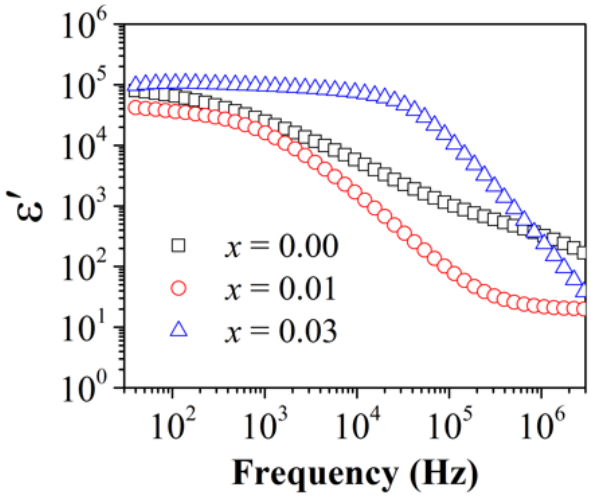

Figure 5 Frequency dependence of ε′ at room temperature of $CuB_{1-x}(Cr_{1/2}Fe_{1/2})_xO_2$ ceramics

At low frequency (< 10^3 Hz), the tanδ of the co-doped $CuB_{1-x}(Cr_{1/2}Fe_{1/2})_xO_2$ ceramics highly increases with decreasing frequency and increasing *x* value. This indicates dc conductivity (σ_{dc}) is the dominant effect. Frequency dependence of the conductivity of all samples was investigated to confirm the effect. As shown in Figure 7, at low frequency the ac conductivity (σ_{ac}) of the $CuB_{1-x}(Cr_{1/2}Fe_{1/2})_xO_2$ ceramics displays relatively little change but it goes up with an increase in frequency. Therefore, the σ_{ac} is frequency independent at low frequency and can be estimated to be equal to σ_{dc}.

From Figure 7, σ_{dc} at room temperature of sample $x = 0.03$ is higher than sample $x = 0.00$ and 0.01. Moreover, this sample has the highest ε′at low frequency accompanied by high σ_{dc} and high tanδ. This analogous behavior was reported in $CuCrO_2$ by Rattanathrum et al. [27]. This suggests that the $CuB_{0.97}(Cr_{1/2}Fe_{1/2})_{0.03}O_2$ sample may have a high polaron concentration that encourages hopping of the polarons within the sample. The giant dielectric permittivity of the $CuB_{1-x}(Cr_{1/2}Fe_{1/2})_xO_2$ ceramics might originate from the motion of charge carriers between Cr^{3+} and Cr^{4+}.

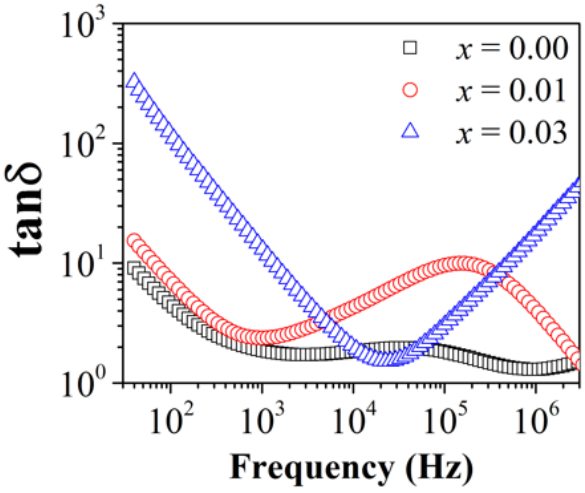

Figure 6 Frequency dependence of tanδ at room temperature of $CuB_{1-x}(Cr_{1/2}Fe_{1/2})_xO_2$ ceramics

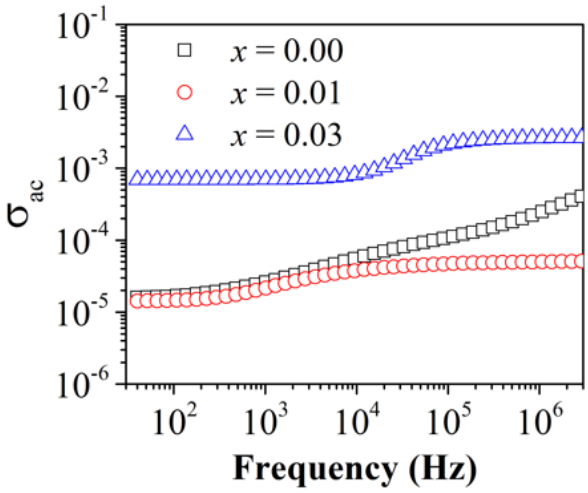

Figure 7 AC Conductivity of $CuB_{1-x}(Cr_{1/2}Fe_{1/2})_xO_2$ ceramics

4. Conclusions

Using a solid-state reaction method, $CuB_{1-x}(Cr_{1/2}Fe_{1/2})_xO_2$ delafossite oxide was successfully prepared. The crystal structure of these materials was revealed by the XRD analysis to be of the delafossite structure space group R-3m. The direct optical band gap was found to decrease from 2.91 eV to 2.85 eV with increasing particle size. The samples upon co-doping with Cr and Fe at room temperature exhibited ferromagnetism, indicated by the presence of a hysteresis loop and the coercivities being about 300 Oe. According to the results of substitution of Cr^{3+}/Fe^{3+} for B^{3+}, it can be concluded that the competition of the number of the M–M pairs and short-range interaction of M–M coupling affect this delafossite's magnetic properties in a mixed fashion. The giant dielectric properties with high ε′ values of about 10^4-10^5 are observed. This behavior can be described by polaron hopping in the bulk ceramics.

5. Acknowledgements

This research was supported by the Basic Research Fund of Khon Kaen University.

6. References

[1] Marquardt MA, Ashmore NA, Cann DP. Crystal chemistry and electrical properties of the delafossite structure. Thin Solid Films. 2006;496(1):146-56.
[2] Kawazoe H, Yasukawa M, Hyodo H, Kurita M, Yanagi H, Hosono H. P-type electrical conduction in transparent thin films of $CuAlO_2$. Nat. 1997;389:939-42.
[3] Nagarajan R, Draeseke AD, Sleight AW, Tate J. P-type conductivity in CuCr1-*x*Mg*x*O_2 films and powders. J Appl Phys. 2001;89(12):8022-5.
[4] Naka-in L, Kamwanna T, Srepusharawoot P, Pinitsoontorn S, Amornkitbamrung V. Effects of Ge substitution on the structural and physical properties of $CuFeO_2$delafossite oxide. Jpn J Appl Phys. 2015;54(4S):04DH10.
[5] Lin F, Shi W, Liu A. Optical bandgap modulation and magnetic characterization of Fe-doped $CuCrO_2$ nanopowders. J Alloy Comp. 2012;529:21-4.

[6] Gao C, Lin F, Zhou X, Shi W, Liu A. Fe concentration dependences of microstructure and magnetic properties for Cu($Cr_{1-x}Fe_x$)O_2 ceramics. J Alloy Comp. 2013;565:154-8.
[7] Lin F, Gao C, Zhou X, Shi W, Liu A. Magnetic, electrical and optical properties of p-type Fe-doped $CuCrO_2$ semiconductor thin films. J Alloy Comp. 2013;581:502-7.
[8] Snure M, Tiwari A. $CuBO_2$: a p-type transparent oxide. Appl Phys Lett. 2007;91:092123.
[9] Santra S, Das A, Das NS, Chattopadhyay KK. $CuBO_2$ Nanonetwork: a novel and significant candidate for photocatalytic dye degradation. Bull Mater Sci. 2018;41:128.
[10] Santra S, Das NS, Chattopadhyay KK. Wide band gap p-type nanocrystalline $CuBO_2$ as a novel UV photocatalyst. Mater Res Bull. 2013;48:2669-77.
[11] Santra S, Das NS, Besra N, Banerjee D, Chattopadhyay KK. Graphene-Anchored p-Type $CuBO_2$ nanocrystals for a transparent cold cathode. Langmuir. 2017;33:9961-71.
[12] Santra S, Das NS, Das B, Banerjee D, Chattopadhyay KK. Synthesis of $CuBO_2$ Nano/Microrods via easy molten salt route and study of its field emission properties. Cryst Growth Des. 2015;15:1518-25.
[13] Santra S, Das NS, Sen D, Chattopadhyay KK. $CuBO_2$: a new highly transparentp-type wide band gap electron field emitter. J Phys Appl Phys. 2014;47:505301.
[14] Santra S, Das D, Das NS, Nanda KK. Effective surface area tuning of noble metal-free $CuBO_2$/rGO Nanohybrid for efficient hydrogen production with “on-off” switching. ACS Appl Energ Mater. 2019;2:260-8.
[15] Jiang T, Bujoli-Doeuff M, Farre Y, Blart E, Pellegrin Y, Gautron E, et al. Copper borate as a photocathode in p-type dye-sensitized solar cells. RSC Adv. 2016;6:1549-53.
[16] Traiphop S, Kamwanna T. Effects of Fe substitution on the structural and magnetic properties of $CuBO_2$ Delafossite oxide. Chiang Mai J Sci. 2020;47:665-85.
[17] Dai H, Ye F, Li T, Chen Z, Cao X, Wang B. Impact of Li doping on the microstructure, defects, and physical properties of $CuFeO_2$ multiferroic ceramics. Ceram Int. 2019;45:24570-7.
[18] Pokhriyal P, Bhakar A, Sinha AK, Sagdeo A. Colossal dielectric permittivity and mechanism of AC conduction in bulk Delafossite $CuFeO_2$. J Appl Phys. 2019;125:164101.
[19] Shah AA, Parveen A, Alvi PA, Azam A. Low temperature synthesis and effect of Co doping on structural, optical and dielectric properties of $CuCrO_2$ hexagonal nanoplates. Ceram Int. 2020;46:19827-34.
[20] Barot N, Mehta PK, Rao A, Thomas R, Kuo YK, Mishra SK. Role of charge doping and distortions on the structural, electrical, and magnetic properties of modified $CuFeO_2$ compounds. J Appl Phys. 2020;127:175704.
[21] Bhattacharya D, Ghoshal D, Mondal D, Das S, Paul BK, Basu M, et al. Colossal dielectric and room temperature ferromagnetic response in CCoTO Delafossite type nanostructure. Solid State Sci. 2020;102:106136.
[22] Oshiro K, Akai K, Matsuura M. Size dependence of polaronic effects on an exciton in a spherical quantum dot. Phys Rev B. 1999;59:10850-5.
[23] Sun L, Zhang R, Wang Z, Cao E, Zhang Y, Ju L. Microstructure, dielectric properties and impedance spectroscopy of Ni doped $CaCu_3Ti_4O_{12}$ ceramics. RSC Adv. 2016;6:55984-9.
[24] Li M, Feteira A, Sinclair DC. Relaxor ferroelectric-like high effective permittivity in leaky dielectrics/oxide semiconductors induced by electrode effects: a case study of CuO ceramics. J Appl Phys. 2009;105:114109.
[25] Nachaithong T, Thongbai P, Maensiri S. Colossal permittivity in ($In_{1/2}Nb_{1/2})_xTi1-xO_2$ ceramics prepared by a glycine nitrate process. J Eur Ceram Soc. 2017;37:655-60.
[26] Traiphop S, Thongbai P, Kamwanna T. Effect of synthesis method on magnetic and dielectric properties of $CuBO_2$ Delafossite oxide. J Aust Ceram Soc. 2020;56:499-505.
[27] Rattanathrum P, Taddee C, Chanlek N, Thongbai P, Kamwanna T. Structural and physical properties of Ge-doped $CuCrO_2$ Delafossite oxide. Ceram Int. 2017;43:S417-22.